ADVANCED ENERGY MATERIALS
www.advenergymat.de

MnAl Layered Double Hydroxides: A Robust Host for Aqueous Ammonium-Ion Storage with Stable Plateau and High Capacity

*Qiang Liu, Fei Ye, Kailin Guan, Yunting Yang, Hongliang Dong, Yuping Wu, Zilong Tang, and Linfeng Hu**

Rechargeable aqueous batteries based on ammonium-ions shows great potential in low-cost energy storage systems owing to their prominent superior characteristics, including ultrafast kinetics, long-term lifespan, and environmental friendliness. Nevertheless, their development is severely challenged by the fact that the as-reported cathode materials generally fail to satisfy the requirements on high capacity and stable working voltage simultaneously. Herein, the first NH_4^+ storage behavior in a MnAl layered double hydroxide (LDH) series is reported. Intriguingly, stable working voltage at 0.2 V is observed in the optimized Mn_3Al_1-LDH sample with a high discharge capacity of 183.7 mAh g^{-1} at 0.1 A g^{-1}. When assembling the rocking-chair battery using a 3,4,9,10-perylenetetracarboxylic diimide anode, the full battery delivers a high energy density of 45.8 Wh kg^{-1}, surpassing most of its recently reported counterparts. A rapid amorphization conversion of the LDH cathode during the first charge process is revealed, which should be beneficial to NH_4^+ isotropic transport accompanied by a highly reversible building/breaking process of hydrogen bonds. The results realize a novel layered inorganic cathode material with superior performance for aqueous ammonium-ion batteries, and the amorphization conversion to facilitate ion storage provides new insight into electrode design for aqueous batteries.

1. Introduction

Rechargeable batteries beyond lithium-ion chemistry have attracted tremendous research interest due to the dramatic development of commercial lithium-ion batteries intensifies the exploitation of lithium resources. Up to date, various batteries beyond lithium-ion based on other metal-ion charge carriers (Na^+, K^+, Mg^{2+}, Ca^{2+}, Zn^{2+}, Al^{3+}) have been widely developed.[1–6] Compared with the metal-ions, the non-metallic charge carriers exhibit lighter molar mass, smaller hydrated ion size, and fast ion diffusion ability in aqueous electrolytes.[7,8] More importantly, non-metallic cation batteries offer advantage on superior long-term lifespan than the metal-ion batteries originating from the absence of dendritic growth behavior during the charge/discharge cycles. However, the battery construction from non-metallic cation as the charge carriers has been neglected and rarely developed.

Most recently, some non-metallic cations, e.g, proton (H^+),[9] hydronium (H_3O^+),[10] and ammonium-ions (NH_4^+),[11] have been regarded as charge carriers in aqueous energy storage field. Especially, NH_4^+ delivers some unique properties such as the smallest hydrated ionic size to facilitate fast diffusion in aqueous electrolyte.[12–14] Compared with proton and hydronium, NH_4^+ is less corrosive and suffers less hydrogen evolution.[15] Ji's groups first constructed the "'rocking-chair"' battery for ammonium-ion storage using metal-organic compound, Prussian blue analogues (PBAs) $[(NH_4)_{1.47}Ni[Fe(CN)_6]_{0.88}$, as the cathode with outstanding cycle stability and rate performance in 2017.[16] Although PBAs display a high discharge plateau at 0.83 V, its discharge capacity less than 60 mAh g^{-1} drastically limits the battery energy density. Subsequently, some inorganic oxides, including layered V_2O_5,[17] hexagonal MoO_3,[18] MnO_x[19] have also been developed as electrode materials for NH_4^+ storage with much enhanced specific capacity. Unfortunately, they generally suffer from the absence of a stable voltage plateau. Therefore, most of the reported cathode materials for aqueous ammonium battery generally fail to satisfy the requirements on high capacity and stable working voltage simultaneously up to date.

Q. Liu, F. Ye, K. Guan, Y. Yang, L. Hu
School of Materials Science and Engineering
Southeast University
Nanjing 211189, P. R. China
E-mail: linfenghu@seu.edu.cn
H. Dong
Center for High Pressure Science and Technology Advanced Research
Shanghai 201203, P. R. China
Y. Wu
School of Energy and Environment
Southeast University
Nanjing 211189, P. R. China
Z. Tang
State Key Laboratory of New Ceramics and Fine Processing
School of Materials Science and Engineering
Tsinghua University
Beijing 100084, China
The ORCID identification number(s) for the author(s) of this article can be found under https://doi.org/10.1002/aenm.202202908.

DOI: 10.1002/aenm.202202908

Undoubtedly, it is very desired and still challenging to discover novel materials combined these two merits together toward high-performance rechargeable ammonium-ion batteries.

Layered double hydroxides (LDHs) are a class of lamellar compounds that consist of positively charged brucite-like host layers and hydrated exchangeable anions located in the interlayer gallery for charge balance.[20] LDHs have achieved special attention on electrochemical pseudocapacitors and OER electrocatalysts owing to their unique layered structure and abundant electrochemical redox activities.[21,22] Recently, the application of LDH electrode in lithium–sulfur batteries [23] and rechargeable zinc ion batteries [24] has also been developed. However, to the best of our knowledge, there is still no report on the aqueous ammonium-ion battery based on LDHs. Since Mn is generally the active species for aqueous ammonium-ion storage,[19] and the amphoteric feature of Al^{3+} is crucial for high-quality LDH crystallization,[20] we consider whether high-performance ammonium-ion storage could be developed in MnAl-LDH series.

Inspired by this consideration, herein, we reported the first NH_4^+ storage behavior in this MnAl layered double hydroxide series. Intriguingly, stable working voltage at 0.2 V has been observed in the optimized Mn_3Al_1-LDH sample with a high discharge capacity of 183.7 mAh g^{-1} at 0.1 A g^{-1}, which is more appealing compared with all inorganic and organic compounds reported recently. Additionally, a lifespan over 400 cycles with a capacity retention of 81% has also been achieved. When assembling the rocking-chair battery using 3,4,9,10-perylenetetracarboxylic diimide (PTCDI) anode, the full battery delivers a high energy density of 45.8 Wh kg^{-1}, surpassing the counterparts recently reported. We revealed a rapid amorphization conversion of our LDH cathode during the first charge process, which would facilitate the NH_4^+ isotropic transport accompanied by a highly reversible building/breaking process of hydrogen bonds.

2. Results and Discussion

2.1. Structure and Morphology

Brown MnAl-LDH samples (molar ratio: Mn:Al = 3:1) were prepared via a conventional co-precipitation strategy as reported previously (**Figure 1**a).[25] All diffraction peaks in the X-ray Diffraction (XRD) pattern well match a hexagonal LDH phase (JCPDS No. 51–1529), demonstrating the high purity of the sample. The sharp and symmetric (002) diffraction peak indicates an interlayer spacing of 7.5 Å (Figure 1c). The scanning electron microscopy (SEM) and transmission electron microscopy (TEM) images of MnAl-LDH nanosheets in Figure 1b,d confirms a morphology of semitransparent, hexagonal nanosheets with an average lateral size of 0.5–2.0 μm. 2D lattice fringe was clearly observed in the corresponding high-resolution transmission electron microscopy (HRTEM) image, the 0.27 nm spacing of which agrees well with the separation of {200} planes (Figure 1e). The sharp hexagonally arranged diffraction spots of the [002] zone axis in the selected area electron diffraction (SAED) pattern taken from an individual LDH sheet demonstrates its single crystal feature with (002) top surface (Figure 1f). In addition, Al, Mn, and O elements are homogeneously distributed in each individual platelet as confirmed by the energy dispersive spectrum (EDS) mapping result in Figure 1g–j. All of the aforementioned characterizations demonstrate that high-quality MnAl-LDH sample has been successfully obtained.

2.2. Ammonium-Ion Storage Behavior

Subsequently, we tried to exploit the ammonium-ion storage behavior in the as-prepared MnAl-LDH by a Swagelok three-electrode configuration, in which the Mn_3Al_1-LDH severed as the working electrode, a graphite foil with an excess of storage capacity serves as the counter electrode, and a saturated Ag/AgCl electrode acts as the reference electrode (E = 0.197 V versus standard hydrogen electrode, SHE), respectively. **Figure 2**a shows the cyclic voltammograms (CV) curves of our MnAl-LDH electrode in 0.5 M $(NH_4)_2SO_4$ aqueous electrolyte at -0.2–1.0 V. One can see a pair of anodic/cathodic peaks at 0.10 and 0.50 V (versus Ag/AgCl), respectively, which could be attributed to the reversible NH_4^+ insertion/extraction in the LDH host. The CV curves overlap well in the first three cycles, implying the high reversibility of the electrochemical process. We further optimized the battery performance by the regulation of electrolyte salt compositions. As depicted in Figure S1 (Supporting Information), four different electrolyte solutions of 1.0 M NH_4Cl, 0.5 M $(NH_4)_2SO_4$, 1.0 M $NH_4CF_3SO_3$, and 1.0 M CH_3COONH_4 were selected respectively to keep the ammonium-ion concentration at 1.0 M. It is clear that our MnAl-LDH cathode exhibits the highest capacity of 294.7 mAh g^{-1} in CH_3COONH_4 electrolyte, which should be attributed to the strong coordination effect of acetate ions as reported most recently[11] (capacity order: CH_3COONH_4 > $NH_4CF_3SO_3$ > NH_4Cl > $(NH_4)_2SO_4$). However, a drastic capacity fading was observed in CH_3COONH_4 electrolyte, and the battery using $(NH_4)_2SO_4$ electrolyte delivers the most stable long-term lifespan. Such a high electrochemical stability and compatibility in $(NH_4)_2SO_4$ electrolyte has also been observed in recent aqueous manganese-ion batteries reported by Niu's group.[26] We further clarify the salt concentration influence on the battery performance by carefully controlling the $(NH_4)_2SO_4$ concentration at 0.25, 0.50, 1.0, 2.0 M, and 5.0 M, respectively. The battery showed an apparent capacity rise with the gradual increase of $(NH_4)_2SO_4$ concentration from 0.25 M to 0.50 M. This phenomenon should be ascribed to desolvation of NH_4^+ become more difficult at a low salt concentration, resulting in a limited migration rate of hydrated NH_4^+.[27] However, further increase in this concentration after this threshold value gave rise to a capacity fading (Figure S2, Supporting Information). Especially, the Mn_3Al_1-LDH cathode in 5.0 M $(NH_4)_2SO_4$ electrolyte just exhibited a much lower discharge capacity of 61.7 mAh g^{-1}. Furthermore, long-term cycling test also reflects a severe capacity decay in this high-concentration electrolyte.

Figure 2b delivers galvanostatic charge/discharge (GCD) curves at a current rate of 0.1 A g^{-1}. Interestingly, very stable charge/discharge plateaus have been observed at 0.49–0.53 and 0.10–0.25 V, respectively, which is well in accordance with the above CV curves. It is noteworthy that this phenomenon is remarkably different with other inorganic materials recently developed for ammonium-ion storage including V_2O_5,[17]

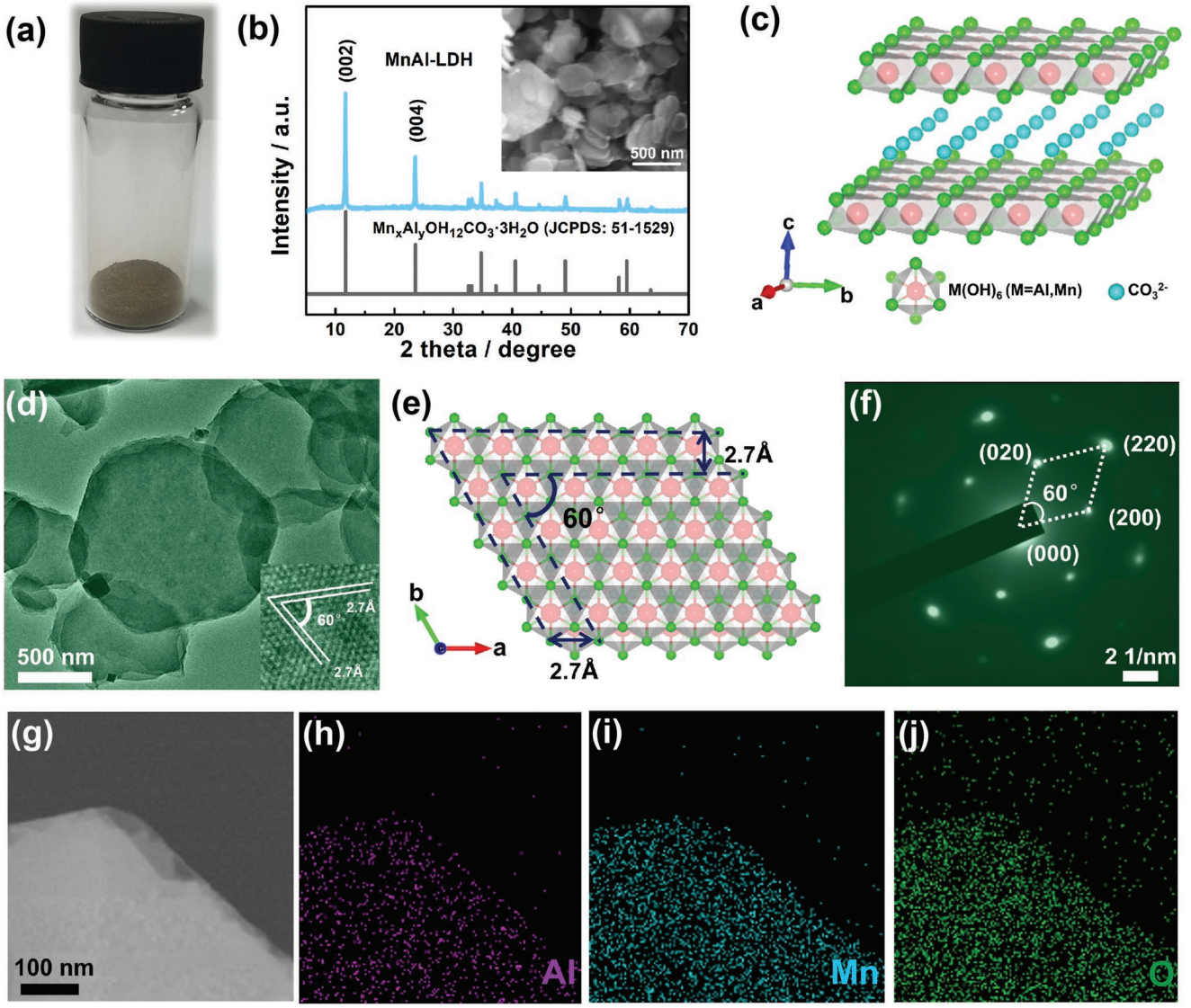

Figure 1. a) Optical photograph of the as-prepared brown Mn_3Al_1-LDH powder. b) XRD pattern of Mn_3Al_1-LDH powder sample with characteristic SEM images inserted. c) Crystal structure and d) TEM image with corresponding HRTEM image inserted. e) Top-view atomic configuration of LDH (002) plane. f) The corresponding SAED pattern. g–j) EDS mapping of Al (purple), Mn (blue), and O (green) in the single sheet, respectively.

MoO_3,[18] MnO_x,[19] etc., of which the linear charge/discharge profiles without the presence of stable discharge plateaus.[28] On the other hand, known that such a stable discharge plateau has also been realized in metal-organic compounds PBAs such as $Fe[Fe(CN)_6]_{0.88}\cdot\square_{0.12}\cdot 2.8H_2O$,[29] $(NH_4)_{1.47}Ni[Fe(CN)_6]_{0.88}$,[30] and some organic materials including Alloxazine, Polyimide (PI), etc.[31–35] However, these metal-organic materials generally show a much smaller capacity than our LDH sample as shown in Figure 2c. It is clear our LDH cathode is more appealing compared with the various conventional cathode materials including both inorganic oxides and metal-organic PBA compounds reported recently.

The ammonium-ion diffusion kinetics in our MnAl-LDH host was identified by a galvanostatic intermittent titration technique (GITT) as shown in Figure 2d. Strikingly, a high ion diffusion coefficient of 1.3×10^{-9} cm^2 s^{-1} has been detected at the discharge plateau stage. To further reveal the charge storage kinetics, CV scans at various scan rates were conducted as shown in Figure 2e. There is very slight shape distortion of the CV curves as the scan rate increases from 0.2 to 1.0 mV s^{-1}. In principle, the peak current (i) is determined by the sweep rate (v) through the following equation:

$$i = av^b \quad (1)$$

where both a and b represent adjustable parameters.[36,37] As shown in the inset of Figure 2e, the coefficients b value of peak A and B are determined to be 0.68 and 0.95, respectively, manifesting that the electrochemical reactions are controlled by both capacitor-like process and ion-diffusion process.[38] Quantitative analysis was carried out to calculate the fraction of current contributed by capacitor-like process and ion-diffusion process according to the following equation:[39]

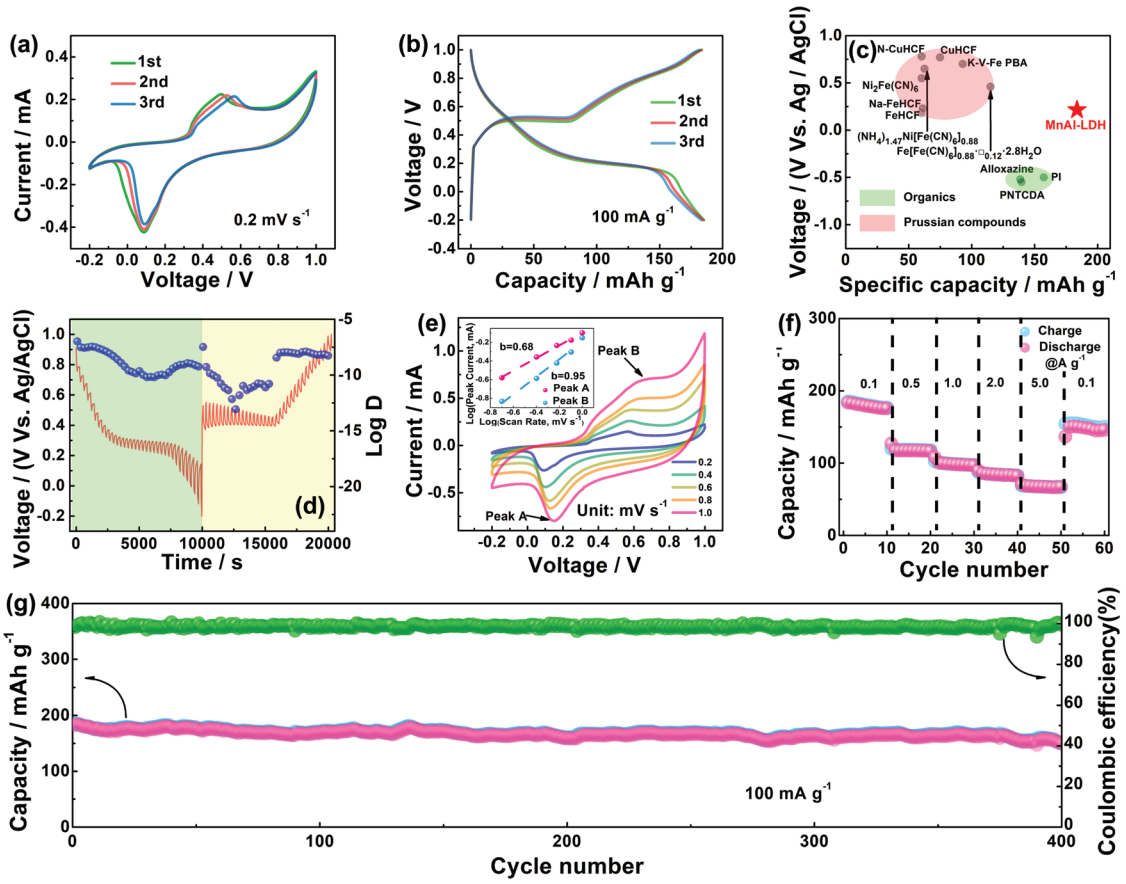

Figure 2. a) Typical CV curves of the LDH cathode for the initial three cycles at 0.2 mV s^{-1}. b) GCD voltage profiles at 0.1 A g^{-1} in 0.5 M $(NH_4)_2SO_4$ electrolyte. c) Comparison of the discharge voltage plateau and specific capacity between our LDH nanosheets and previously reported cathodes for aqueous ammonium battery. d) GITT profiles in the second cycle and the calculated ammonium-ion diffusion coefficient. e) CV curves at different scan rates from 0.2 to 1.0 mV s^{-1}. Inset is the log *i* versus log *v* plots based on the CV profiles at two different oxidation/reduction states. f) Rate-performance and g) long-term cycle performance at 0.1 A g^{-1}.

$$i(v) = k_1 v + k_2 v^{1/2} \quad (2)$$

The contribution ratios for the capacitive current in comparison with the total current are 26%, 38%, 46%, 49%, and 55% at a scan rate of 0.2, 0.4, 0.6, 0.8, and 1.0 mV s^{-1} (Figure S3, Supporting Information), respectively, and it keeps increasing along with the increase of voltage scan rates.[1,40]

Rate-capability and long-term cycling stability are another two essential factors to evaluate the performance of rechargeable batteries. As shown in Figure 2f, our MnAl-LDH electrode delivers a reversible specific capacity of 183, 127, 108, 89, and 70 mAh g^{-1} at the current densities of 0.1, 0.5, 1.0, 2.0, and 5.0 A g^{-1}, respectively. The capacity recovered to 150 mAh g^{-1} when the current density returned back to 0.1 A g^{-1}, indicating the excellent chemical reversibility of our sample. Long-term cycling stability over 400 cycles has also been confirmed at 0.1 A g^{-1} as shown in Figure 2g. The LDH cathode can deliver a 81% capacity retention (149.1 mAh g^{-1}) after 400 cycles with Coulombic efficiency close to 100%.

It is well-known that the M^{3+}/M^{2+} species ratio in LDH lattice can be discretionarily regulated by changing the ratio of initial reactants. Accordingly, the battery performance was further studied through the Mn/Al ratio tunning in our Mn-Al LDH sample. **Figure 3**a shows the XRD patterns of a series of Mn_xAl_1-LDH samples with various Mn/Al ratio from 1.0 to 4.0, suggesting that pure LDH phases were successfully synthesized at different ratios other than the Mn/Al = 1.0 case. The Mn_xAl_1-LDH (x = 1, 2, 3, 4) series delivers a discharge capacity of 97.8, 163.6, 183.7, and 142.5 mAh g^{-1} at 100 mA g^{-1} within the voltage range of –0.2–1.0 V, respectively (Figure 3c). Figure 3d presents the electrochemical impedance spectroscopy (EIS) spectra of our Mn_xAl_1-LDH series. Based on the semicircles in the high-frequency region (Table S1, Supporting Information), the Mn_3Al_1-LDH (R_{ct} value is 58 Ω) sample is more conducive to enable rapid charge transfer than other Mn_xAl_1-LDHs (R_{ct} value of Mn_1Al_1-LDH, Mn_2Al_1-LDH, and Mn_4Al_1-LDH is 80, 75, and 79 Ω, respectively). Generally, the slope in the low-frequency regions is inversely proportional to ion diffusion resistance.[41] Thus, it is rational that the order of ammonium-ion diffusion resistance in our LDH series is as follows: Mn_3Al_1-LDH < Mn_4Al_1-LDH < Mn_2Al_1-LDH < Mn_1Al_1-LDH. The Mn_3Al_1-LDH sample also delivers a superior cycling stability with the highest capacity retention of 81% over

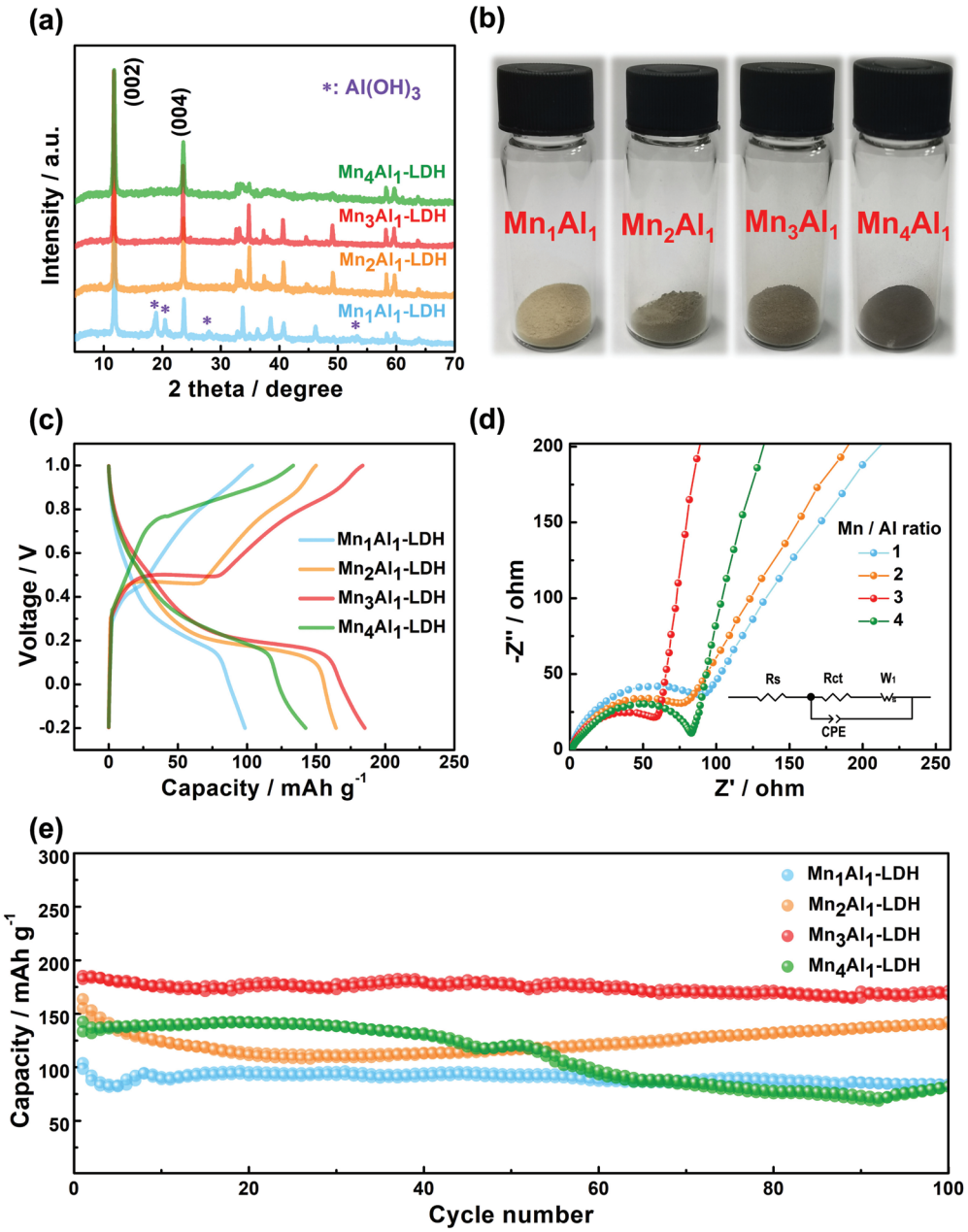

Figure 3. a) XRD patterns and b) optical photograph of the Mn_xAl-LDH series with different Mn/Al ratio from 1.0 to 4.0, respectively. $Al(OH)_3$ impurity has been observed in the Mn/Al = 1.0 case due to excess aluminum species in the sample. c) Typical GCD curves at 0.1 A g^{-1}. d) EIS spectra of Mn_xAl-LDH electrode. e) Cycle performance at 0.1 A g^{-1} of the Mn_xAl_1 LDH series.

400 cycles compared with other ones (Figure 3e; Figure S4, Supporting Information). Considering the active metal is Mn for the reversible ammonium-ion storage as discussed below, it is easy to understand that excessive Al species in the MnAl-LDH host results in the reduction of specific capacity.[42] Meanwhile, Al species also plays a crucial role in the immobilization of LDH framework, and high-quality LDH samples with non-Al^{3+} host layer composition are difficult to realize in general.[43] Consequently, when Al^{3+} concentration in the LDH framework is too low, the appearance of $Al(OH)_3$ impurity and a remarkable decrease in capacity has been observed. All of the results clarify that Mn/Al ratio of 3.0 should be the best choice for high-capacity and stable ammonium-ion storage.

2.3. Ammonium-Ion Storage Mechanism

The encouraging battery performance on stable working voltage and high capacity observed in our Mn_3Al_1-LDH host induces us to further unveil its underlying energy storage mechanism in one charge/discharge/charge cycle (charged first). Fifteen statuses at this charge/discharge/charge cycle were carefully selected in **Figure 4**a for various ex situ characterizations. Ex

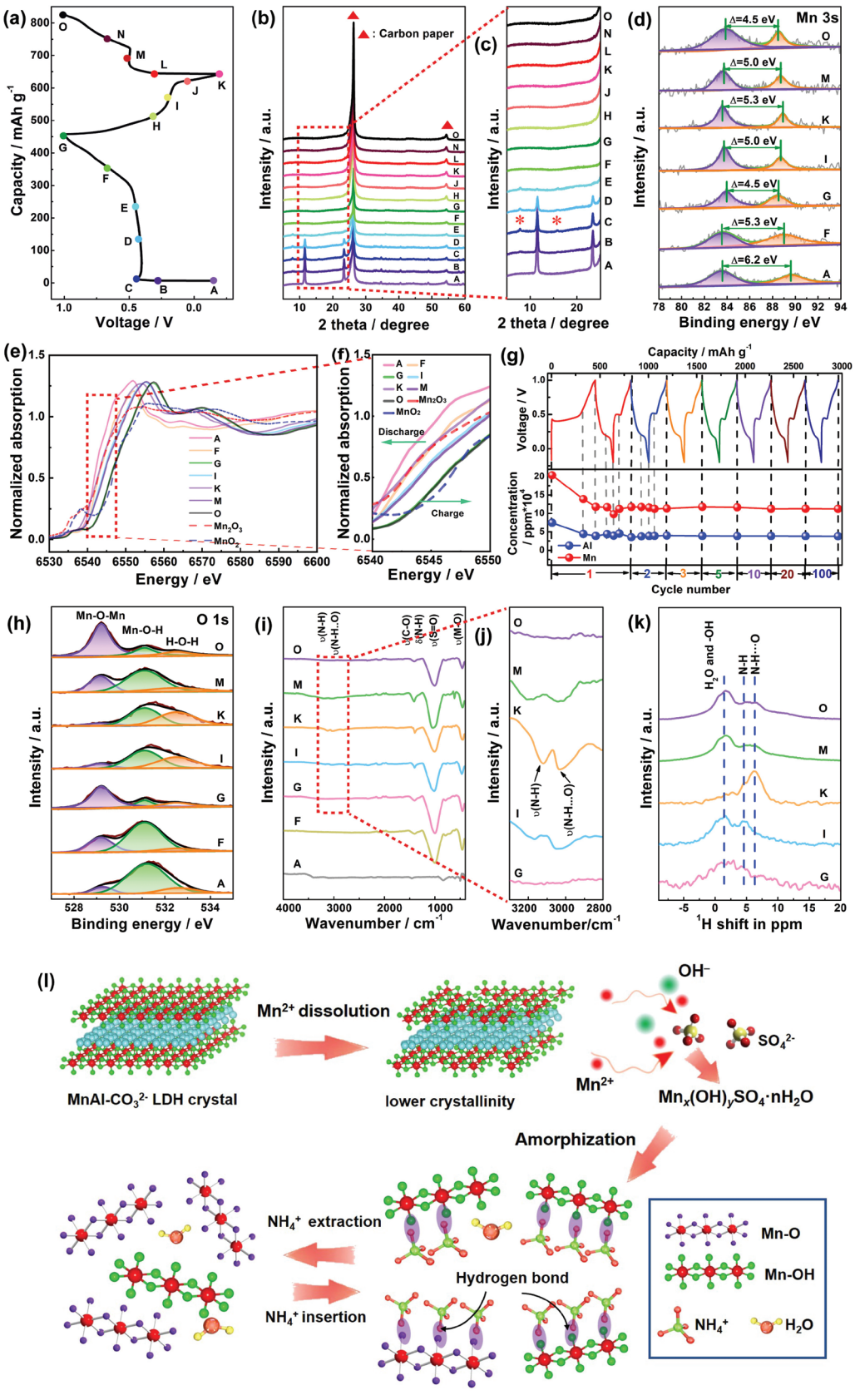

Figure 4. a) GCD curves to marked out the traced states from A to O. b,c) Ex situ XRD pattern, d) Mn 3s d) and h) O 1s XPS spectra. e,f) the X-ray absorption near edge structure characterizations data. g) ICP results. i,j) FTIR, k) solid-state ^{1}H NMR spectra corresponded to different charge/discharge states in a). l) Schematic illustration of the ammonium-ion storage mechanism in the MnAl-LDH host.

situ XRD measurement was performed to reveal the detailed structural evolution (Figure 4b, c). One can see the diffraction peaks at 11.6 and 23.3°, corresponding to the (002) and (004) planes of Mn_3Al_1-LDH phase respectively, become much weaker from A to E and completely disappear at F state. Synchronously, two new diffraction peaks located at 7.8° and 15.6° marked with * in Figure 4c (see the enlarged pattern in Figure S6, Supporting Information) emerge at B state, which can be indexed to $Mn_x(OH)_ySO_4\cdot 5H_2O$ phase.[44] The appearance of $Mn_x(OH)_ySO_4\cdot nH_2O$ byproduct implies the dissolution of Mn species in the LDH sample, which was further supported by tracking the Mn concentration in the electrode during this charge process from inductively coupled plasma (ICP) measurement (Figure 4g). When the battery was deeply charged to 0.65 V (F state in Figure 4c), the diffraction peaks from LDH completely disappeared and only the peaks from carbon-paper collector were detected, demonstrating a conversion from the initial highly crystallized Mn_3Al_1-LDH to the amorphous phase. The characteristic peaks of $Mn_x(OH)_ySO_4\cdot 5H_2O$ cannot be observed after F state as well, which is should be caused by the successive Mn species oxidation process as discussed below. Note that the cathode well-maintained this amorphous phase after this point, and the amorphous feature has been identified by the ex situ XRD results at varied fully charged states of the subsequent 5, 10, 50, 100, 200, and 400 cycles (Figure S7, Supporting Information).

To further clarify the origin for the as-observed capacity, Mn K-edge X-ray absorption near edge structure (XANES) characterization of the Mn_3Al_1-LDH cathode at different statuses was carried out using commercial MnO_2 and Mn_2O_3 as reference samples. As shown in Figure 4e,f, the Mn K-edge gradually shifts toward higher energy from A to G point, indicating the increase of the average Mn valence state and the oxidation of Mn species in the cathode. Note that the Mn K-edge at G point is very close to that of the commercial MnO_2, demonstrating the Mn valence state is +4 at this status. Therefore, it is rational that the mechanism for the first charged capacity is originated from the oxidation of Mn species from Mn^{2+} in initial LDH cathode to Mn^{4+}. During the following discharge process from G to K point, the Mn K-edge recover back to the low valence state close to that of commercial Mn_2O_3, suggesting the redox reaction from Mn^{4+} to Mn^{3+} during the discharging (Figure S8, Supporting Information). Subsequently, from point K to point O, the edge shift is analogous to the case in the first charging process accompanied with the oxidation of Mn species to Mn^{4+} (Figure S8c, Supporting Information). Accordingly, based on this Mn K-edge XANES spectra, the Mn valence evolution can be summarized as follows:

the first charge process: $Mn^{2+} \rightarrow Mn^{4+} + 2e^-$

the following discharge/charge process: $Mn^{4+} + e^- \leftrightarrow Mn^{3+}$

Ex situ X-ray photoelectron spectra (XPS) characterization was carried out to clarify the chemical compositions and valence state evolution of our LDH active material (Figure 4d,h). As depicted in Figure 4d, the peak separation of the Mn 3s spectra changes from 6.0 eV (open circuit potential state A) to 5.3 eV (charge plateau state F), and then to 4.5 eV (full charged state G). In general, the appearance of 5.3, 4.5 eV peak separation provides evidence for the existence of Mn^{3+}, Mn^{4+}, respectively.[45,46] Consequently, it is rational that Mn valence state in the LDH electrode increased from initial +2.2 to +3.0 and finally to +3.9 from A to G point.[46] Subsequently, during the following discharge/charge cycle, the Mn 3s spectra depicts a peak separation of 5.0 eV (discharge plateau state I), 5.3 eV (fully discharge state K), 5.0 eV (charge plateau state M) and then returns back to 4.5 eV (fully charge state O), respectively. The result indicates the reversible transformation from Mn^{4+} to Mn^{3+} in the electrode after the first charge process.[46] The corresponding O 1s spectra are presented in Figure 4h. All of the O 1s peaks from point A to O can be deconvoluted into three peaks at ≈529.2, ≈531.1, and ≈532.5 eV, corresponding to metal oxide (Mn-O-Mn), metal hydroxide (Mn-O-H), and adsorbed crystal water (H-O-H), respectively.[47,48] One can see the peak intensity of the Mn–O–Mn bond (529.2 eV) gradually increases accompanied with a simultaneous reduction of the Mn–O–H bond (529.2 eV) intensity from point A to G, suggesting the Mn_3Al_1-LDH were transformed into some amorphous metal oxides during the first charge process.[49] During the following discharge process from point G to K, the peak for the Mn–O–Mn bond shows a reduction on intensity and mostly disappear upon fully discharging at the state K. Meanwhile, the Mn–O–H bond peak gradually become prominent and exhibits the highest intensity at K state. Upon recharged to 1.0 V (from state K to O), the peak intensity of Mn–O–Mn bond recovers to its initial state. On the other hand, the peak of H–O–H bond originated from crystal water shows a similar tendency to Mn–O–H bond during the discharge and charge process, respectively.

To further understand where is Al species in our LDH phase going during this electrochemical process, XPS characterization of the LDH cathode at three typical statuses (A, B, C point in Figure S9, Supporting Information) was performed. Ar ion etching technology was used during the XPS characterization to record the XPS spectra at various depths of the Mn_3Al_1-LDH sample. As shown in Figure S9b (Supporting Information), the characteristic XPS peak located at 74.2 eV can be ascribed to the Al 2p spin-orbital. From A to C point, the signal of Al 2p peaks exhibit no apparent discrepancy at two different depths of the Mn_3Al_1-LDH sample (10, 50 nm away from the sample surface, respectively). This result may verify the uniform distribution of Al species along the depth of the LDH phase, and Al element does not participate in the redox reaction. Note that the Al 2p peak intensity of B, C point is much lower than that of A point, suggesting the possible Al species dissolution during the first charged process. Furthermore, the concentration of Al species in LDH electrode during monitored by ICP measurement is also shown in Figure 4g. The concentration of Al species drastically declined in the initial charge process, also confirming the dissolution of Al species. However, this concentration becomes stable during the following discharge/charge cycles, suggesting the Al species dissolution was remarkably alleviated after the first cycle.

SEM observations were used to characterize the morphology evolution of the LDH nanosheets at different depths of charge and discharge. Accompanied with the as-revealed rapid amorphous phase transformation, our LDH sample lost its 2D nanosheet morphology and completely evolved into 3D microspheres assembled by massive wrinkled nanosheets (see Figure S10, Supporting Information). This

microsphere-like morphology was well-maintained during the following 100 charge/discharge cycles. TEM observation of the active material after one cycle and 100 cycle respectively also confirms the wrinkled nanosheets in the microsphere-like morphology, and its amorphous future was further confirmed by the characteristic halo ring pattern in the corresponding SAED pattern (Figures S11 and S12, Supporting Information).

Another question is whether NH_4^+ is indeed inserted into the amorphous structure after the irreversible amorphization and which kind of chemical bonding has been formed during this electrochemical process. The EDS mapping from TEM observation after 100 charge/discharge cycles indicates a homogeneous distribution of Mn, Al, O, and S elements in the nanosheets. More importantly, N element can be clearly detected in the electrode after first cycle in the mapping, providing the evidence that NH_4^+ has been inserted into the electrode. On the other hand, ex situ Fourier transform infrared (FTIR) spectra further verify the hydrogen bond formation during the ammoniation/ de-ammoniation cycles (Figure 4i,j). The FTIR peaks ≈3300—3500 cm^{-1} is ascribed to the –OH bands from the OH group in our MnAl-LDH structure,[50] which gradually disappear during the first charge process from A to G state, corresponding to the aforementioned amorphous transformation and layered structure collapse accompanied with the dissolution of Mn species in LDH. Meanwhile, a strong stretching vibration peak ascribed to S=O band at 1000 cm^{-1} emerges at the F state,[51] which could be originated from SO_4^{2-} groups due to the formation of $Mn_x(OH)_ySO_4 \cdot 5H_2O$.[44] There are two characteristic peaks for the vibrations of N-H in NH_4^+ at ≈3050 and 3180 cm^{-1} at the I state, where the former is ascribed to the N-H stretching peak in which the H bonded with the Mn-O host, and the latter is the N-H stretching peak including non-bonded H.[17–19] Specifically, their intensities gradually increase from I state to K state, suggesting the ammonium-ions were inserted into our cathode through H-bonding with Mn-O host. Subsequently, they decrease from K to M state and completely disappear at O state, which can be ascribed to the de-ammoniation processes accompanied with hydrogen bonds broken.

Solid-state ^1H nuclear magnetic resonance (NMR) was also conducted to quantitative probe protonic species at different discharge/charge depths as shown in Figure 4k. The resonances at ≈0 – 2.2 ppm are assigned to crystal water and the abundant –OH groups in the LDH structure.[19] There are two main peaks centered at ≈6.4 and 4.5 ppm at the fully discharged state (point K), which could be ascribed to H-bonded and non-bonded hydrogen in NH_4^+.[52] Upon discharge to –0.2 V (from G to K), the resonance intensity of the ammonium-ions increases substantially, which corresponds to the insertion of NH_4^+ into the MnAl-LDH host. When charging to 1.0 V (from K to O), the resonance gradually become weaker and finally return to its initial state, which can be attributed to the extraction of NH_4^+ during the charge process.[19]

Consequently, all the above ex situ measurements reveal a highly reversible building/breaking process of hydrogen bonds after the irreversible amorphization of the MnAl-LDH framework. Previous studies have confirmed that the dehydrated ammonium-ions can twist and rotate to maintain a subset of coordinated H bonds with adjacent oxygen atoms from the either crystal water or lattice oxygen, and revealed a monkey swinging mechanism that the NH_4^+ twists to disconnect one of its trailing H bonds and reaches forward to a new O bond ahead.[15] In our case, benefiting from long-range disorder and isotropic characteristics of the as-transformed amorphous structure, fast transport kinetics with a high NH_4^+ diffusion coefficient of 1.3×10^{-9} cm^2 s^{-1} has been achieved in Figure 2d.

2.4. Full-Battery Construction

We attempt to construct a full cell from our LDH cathode toward a more practical application. **Figure 5**a illustrates the schematic configuration of the full cell, using commercial PTCDI as the anode material owing to its suitable reduction potential (see Figure S13, Supporting Information). Typical CV profiles of this MnAl-LDH / 0.5 M $(NH_4)_2SO_4$ / PTCDI full cell at a current density of 0.2 mV s^{-1} delivers a pair of anodic/cathodic peak at ≈0.6/1.4 V (Figure S14, Supporting Information). GCD profiles of the as-constructed battery in Figure 5b verify an average operating voltage of 0.78 V and a specific capacity of 57.7 mAh g^{-1} (based on the total active mass of cathode and anode). The battery shows a rate-capacity of 65, 47, 45, 40, and 35 mAh g^{-1} at 0.1, 0.5, 1.0, 2.0, and 5.0 A g^{-1}, respectively, and it recovers to 50 mAh g^{-1} when the current density returns back to 0.1 A g^{-1} (Figure 5c). Long-term cycling identifies a cycle life over 100 cycles at the rate of 0.1 A g^{-1} with a satisfactory capacity retention of 92% and the Coulombic efficiency of ≈98% (Figure 5d). Remarkably, our MnAl-LDH // PTCDI full battery exhibits a high energy density of 45.8 Wh kg^{-1} at a power density of 163.5 W kg^{-1}(based on the total active mass of cathode and anode), suppressing most of the NH_4^+ ion batteries (NHIBs) recently reported involving PTCDI // $NH_4Fe_4[Fe(CN)_6]_3$,[53] Poly(1,5-NAPD) // NiHCF,[54] PANI//CuHCF,[34] etc. (Figure 5e). Figure 5f gives the performance comparison between specific energy and power of the our LDH-based NHIBs and other energy storage devices. Obviously, our aqueous NHIBs with low-cost and environmental friendliness show a much higher specific power than that of Pb-acid batteries and fuel cells, can also deliver superior specific energy to that of the supercapacitors. To further verify the practical application in flexible and wearable device, a soft package of four batteries in series was constructed as shown in Figure 5g, which can easily drive a group of light-emitting diode (LED) indictor under varied bending states (45°, 90°, 135°, and 180°), demonstrating its excellent flexibility and promising wearable potential.

Generally, H^+ insertion/extraction can be observed in aqueous batteries endowing the battery as a dual-ion system. To identify whether the proton insertion is present in our cell, we compared the battery performance in aqueous $(NH_4)_2SO_4$ electrolyte and a H_2SO_4 solution with the same pH value of 4.9. As shown in Figure S15 (Supporting Information), the Mn_3Al_1-LDH // PTCDI full battery in H_2SO_4 electrolyte show almost no capacity on energy storage (≈3 mAh g^{-1}). This result excludes the possibility of H^+ involvement in the energy storage mechanism. Considering the presence SO_4^{2-} group in the $(NH_4)_2SO_4$ electrolyte, we further track SO_4^{2-} evolution

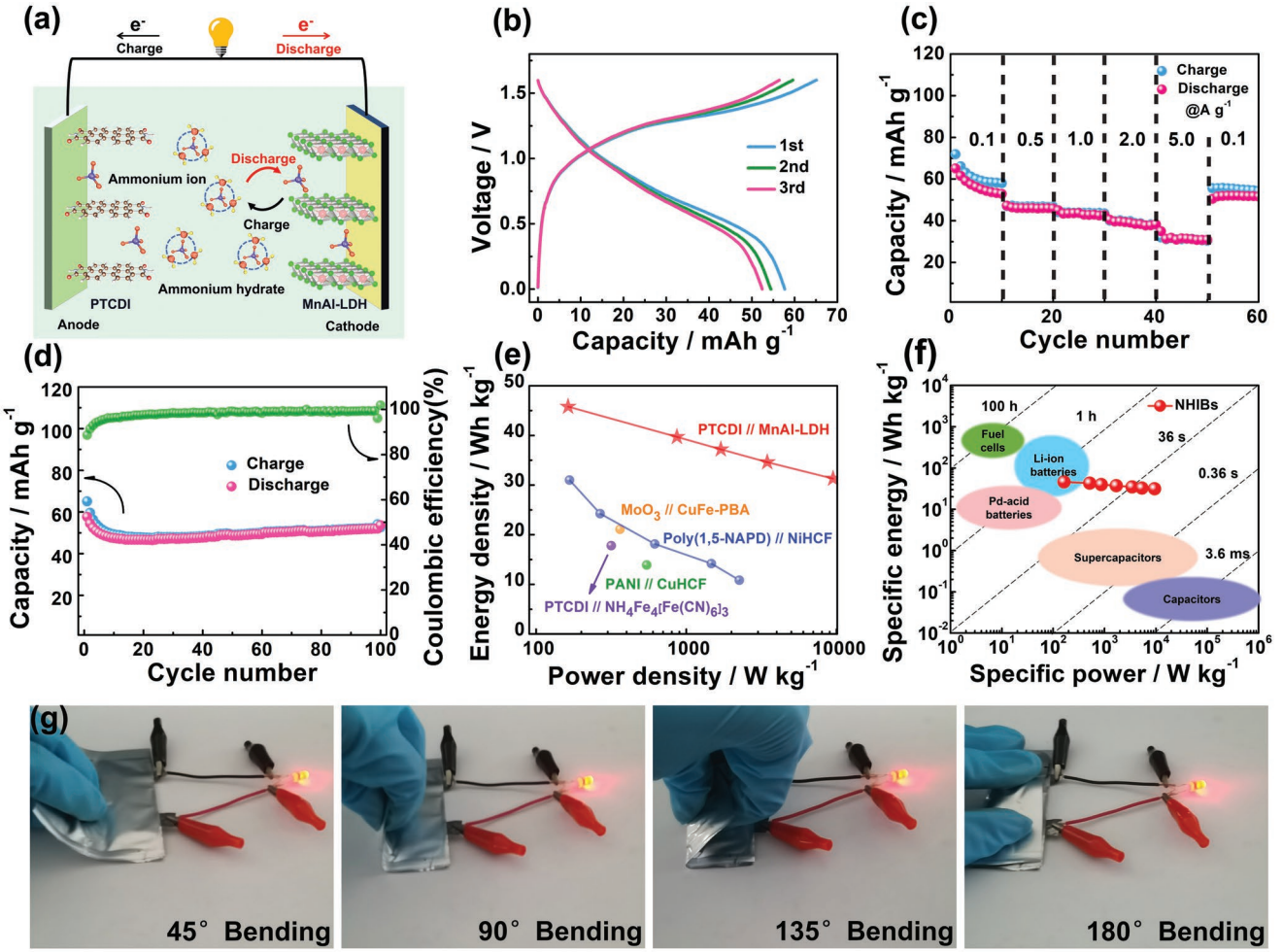

Figure 5. a) Schematic structure of the MnAl-LDH / 0.5 M $(NH_4)_2SO_4$ / PTCDI full battery. b) GCD curves at 0.1 A g^{-1}. c) Rate capability at different rates of 0.1–5.0 A g^{-1}. d) Cycle performance at 0.1 A g^{-1}. e) Ragone plot of our MnAl-LDH cathode and a series of other cathode materials reported previously.[18,34,53,54] f) Ragone plot showing the specific energy and power of the our LDH-based NHIBs with various commercial energy storage devices. g) Soft-packed battery utilized for driving a LED test under varied bending angles.

in PTCDI anode during the ammoniation/ de-ammoniation cycles using ex situ FTIR spectra (Figure S16). However, the characteristic S=O stretching peak ≈1000 cm^{-1} was hardly detected, indicating the SO_4^{2-} group does not participate in electrochemical reactions as charge carriers in the anode side. All results verify that our full-battery device is a typical ammonium-ion battery with NH_4^+ cation as the only charge carrier, and the corresponding electrochemistry reaction equation can be illustrated as follows:

1. LDH cathode:the first cycle charge progress:

$$Mn^{2+}(\text{in crystalline LDH}) \rightarrow Mn^{4+}(\text{in amorphous state}) + 2e^- \quad (3)$$

the subsequent cycles:

$$\text{discharge}: Mn^{4+}(\text{in amorphous state}) + e^- \xrightarrow{\text{ammonium ion insertion}} Mn^{3+}(\text{in amorphous state}) \quad (4)$$

$$\text{charge}: Mn^{3+}(\text{in amorphous state}) \xrightarrow{\textit{ammonium ion extraction}} Mn^{4+} + e^-(\text{in amorphous state}) \quad (5)$$

2. PTCDI anode:[16]

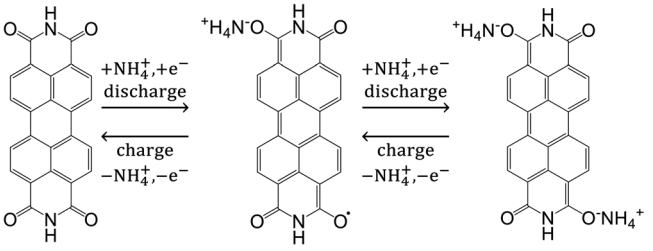

3. Conclusion

In summary, we observed very stable charge/discharge voltage in MnAl-LDH series with a high specific capacity of 183.7 mAh g^{-1} for reversible ammonium-ion storage. A stable lifespan of over 400 cycles with a capacity retention of 81% has also been achieved. When assembling the rocking-chair battery, the LDH-based full battery delivers a high energy density of 45.8 Wh kg^{-1}, surpassing the counterparts recently reported. We revealed a rapid amorphization conversion of

the MnAl-LDH cathode during the first charge process is beneficial to the NH_4^+ isotropic transport in the host accompanied by a highly reversible building/breaking process of hydrogen bonds. Our work demonstrates MnAl-LDHs is a very appealing cathode candidate, and realizes the first inorganic compound with very stable working voltage for NH_4^+ storage. We hope this research could sever as the initiating study of reversible NH_4^+ storage in amorphous structure, and the amorphization conversion to facilitate ion storage can be advantageous in designing other enhanced electrode materials for aqueous energy storage.

4. Experimental Section

Material Synthesis: The co-precipitation strategy was utilized to synthesize of Mn_xAl-LDHs (x = 1, 2, 3, and 4) samples with different Mn/Al molar ratios. First, x mmol $Mn(CH_3COO)_2{\cdot}4H_2O$ and 1 mmol $Al(OH)(CH_3COO)_2$ were dissolved in 200 ml deionized (DI) water to form solution A. Then, 0.53 g Na_2CO_3 and 0.64 g NaOH were added in 25 ml DI water to form solution B. Second, the solution A transferred into a three-neck flask equipped with a reflux condenser and treated with a nitrogen flow for 30 min. Solution B was quickly poured into solution A under magnetometric stirring, and maintained the pH constant (pH = 10.5). Last, it was stirred for 6 h at 95 °C under N_2 atmosphere. The resulting slurry was washed and dried at room temperature for 24 h. The organic solid of PTCDI was a commercially available pigment and was purchased from Aldrich.

Material Characterization: The structure morphology and structure characterization were characterized by, SEM (Zeiss sigma HD), HRTEM, and XRD (Bruker D8-A25 diffractometer using Cu Kα radiation (λ = 1.5406 Å)). The SAED and EDS mapping were carried out during the TEM measurement (JEM-2100F) process to gather detailed information of phase structure and chemical element distribution of the sample. Further information of the chemical bonding condition and the element concentration was recorded by means of XPS (Thermo Fisher 250Xi), FTIR (Bruker TENSOR II), SSNMR (Bruker AVANCE III HD NMR 400 M), and ICP (Agilent 5100).

Electrochemical Measurement: MnAl-LDH cathode for aqueous NHIBs was prepared by mixing as-prepared MnAl-LDH nanosheets, acetylene black, and polyvinylidene fluoride (PVDF) on the basis of a mass ratio of 7:2:1 with the moderate addition of 1-methyl-2-pyrrolidinone (NMP), then coating onto a carbon fiber and during under vacuum at 70 °C for 12 h. The slurry-coated carbon fiber was cut into Φ10 mm electrodes that served as the cathode, while the graphite foil and glass fiber membrane were used as the anode and separator, respectively, and 0.5 M $(NH_4)_2SO_4$ was prepared as the electrolyte. For the as-assembled full-cell device, the mass loading of negative and positive electrodes was ≈4.5 and 1.5 mg cm^{-2}, respectively. The Swagelok cell was assembled in air using the beforehand electrodes and other relevant components. LAND battery test system (CT2001A) was employed to evaluate the electrochemical vcycle performance. GITT was applied to investigate the diffusion kinetics for ammonium-ion. CV and EIS technology were performed on the CHI 660E workstation.

The Fabrication of Pouch Cells: The fabrication process of the pouch cells in the experimental section. Mn_3Al_1-LDH cathode and PTCDI anode for aqueous NHIBs were prepared by mixing active material, acetylene black, and PVDF on the basis of a mass ratio of 7:2:1 with the moderate addition of NMP, then coated onto a carbon fiber cloth (CFC) and during under vacuum at 70 °C for 12 h. The slurry-coated CFC was cut into 1 × 3 cm electrodes, while the glass fiber membrane was used as the separator, and 0.5 M $(NH_4)_2SO_4$ was prepared as the electrolyte. The fully assembled pouch battery was finally sealed with aluminum plastic film as a sandwich structure.

Supporting Information

Supporting Information is available from the Wiley Online Library or from the author.

Acknowledgements

This work was financially supported by the National Key Research and Development Program of China (Grant No. 2021YFB2400400), the Natural Science Foundation of Jiangsu Province (Grants No. BK20211516), the National Natural Science Foundation of China (Nos. 52171203, 51872051), the State Key Laboratory of New Ceramic and Fine Processing of Tsinghua University (No. KF202102), and the Fundamental Research Funds for the Central Universities (2242022R10090). The authors thank the beamline station 4B9A of Beijing Synchrotron Radiation Facility (BSRF) for the help in characterizations.

Conflict of Interest

The authors declare no conflict of interest.

Data Availability Statement

The data that support the findings of this study are available from the corresponding author upon reasonable request.

Keywords

amorphization conversion, aqueous ammonium-ion batteries, discharge plateau, MnAl-LDHs, specific capacity

Received: August 26, 2022
Revised: October 31, 2022
Published online: December 2, 2022

[1] D. L. Chao, S. Z. Qiao, *Joule* **2020**, *5*, 1846.
[2] Q. F. Zhang, X. L. Cheng, C. X. Wang, A. M. Rao, B. A. Lu, *Energy Environ. Sci.* **2021**, *14*, 965.
[3] H. Dong, O. Tutusaus, Y. L. Liang, Y. Zhang, Z. L. Higgins, W. L. Yang, R. Mohtadi, Y. Yao, *Nat. Energy* **2020**, *5*, 1043.
[4] A. Ponrouch, C. Frontera, F. Bardé, M. R. Palacin, *Nat. Mater.* **2016**, *15*, 169.
[5] D. Kundu, B. D. Adams, V. Duffort, S. H. Vajargah, L. F. Nazar, *Nat. Energy* **2016**, *1*, 16119.
[6] M. C. Lin, M. Gong, B. A. Lu, Y. P. Wu, D. Y. Wang, M. Y. Guan, M. Angell, C. X. Chen, J. Yang, B. J. Hwang, H. J. Dai, *Nature* **2015**, *520*, 324.
[7] G. J. Liang, F. N. Mo, X. L. Ji, C. Y. Zhi, *Nat. Rev. Mater.* **2021**, *6*, 109.
[8] X. Y. Wu, J. J. Hong, W. Shin, L. Ma, T. C. Liu, X. X. Bi, Y. F. Yuan, Y. T. Qi, T. W. Surta, W. X. Huang, J. Neuefeind, T. P. Wu, P. A. Greaney, J. Lu, X. L. Ji, *Nat. Energy* **2019**, *4*, 123.
[9] S. T. Wang, H. Jiang, Y. H. Dong, D. Clarkson, H. Zhu, C. M. Settens, Y. Ren, T. Nguyen, F. Han, W. W. Fan, S. Y. Kim, J. N. Zhang, W. J. Xue, S. K. Sandstrom, G. Y. Xu, E. Tekoglu, M. D. Li, S. L. Deng, Q. Liu, S. G. Greenbaum, X. L. Ji, T. Gao, J. Li, *Adv. Mater.* **2022**, *34*, 2202063.
[10] Z. W. Guo, J. H. Huang, X. L. Dong, Y. Y. Xia, L. Yan, Z. Wang, Y. G. Wang, *Nat. Commun.* **2020**, *11*, 959.
[11] D. Yang, Y. Song, M. Y. Zhang, Z. M. Qin, J. Liu, X. X. Liu, *Angew. Chem., Int. Ed.* **2022**, *61*, e202207711.
[12] J. Han, A. Varzi, S. Passerini, *Angew. Chem., Int. Ed.* **2022**, *61*, e202115046.
[13] R. D. Zhang, S. Wang, S. L. Chou, H. L. Jin, *Adv. Funct. Mater.* **2022**, *32*, 2112179.

[14] Z. N. Tian, V. S. Kale, Y. Z. Wang, S. Kandambeth, J. C. Jóźwiak, O. Shekhah, M. Eddaoudi, H. N. Alshareef, *J. Am. Chem. Soc.* **2021**, *45*, 19178.
[15] D. L. Chao, H. J. Fan, *Chem* **2019**, *5*, 1357.
[16] X. Y. Wu, Y. T. Qi, J. J. Hong, Z. F. Li, A. S. Hernandez, X. L. Ji, *Angew. Chem., Int. Ed.* **2017**, *129*, 13206.
[17] S. Y. Dong, W. Shin, H. Jiang, X. Y. Wu, Z. F. Li, J. Holoubek, W. F. Stickle, B. Key, C. Liu, J. Lu, P. A. Greaney, X. G. Zhang, X. L. Ji, *Chem* **2019**, *5*, 1537.
[18] G. J. Liang, Y. L. Wang, Z. D. Huang, F. N. Mo, X. L. Li, Q. Yang, D. H. Wang, H. F. Li, S. M. Chen, C. Y. Zhi, *Adv. Mater.* **2020**, *32*, 1907802.
[19] Y. Song, Q. Pan, H. Z. Lv, D. Yang, Z. M. Qin, M. Y. Zhang, X. Q. Sun, X. X. Liu, *Angew. Chem., Int. Ed.* **2021**, *60*, 5718.
[20] P. J. Sideris, U. G. Nielsen, Z. H. Gan, C. P. Grey, *Science* **2008**, *321*, 113.
[21] Z. C. Pan, Y. C. Jiang, P. Y. Yang, Z. Y. Wu, W. C. Tian, L. Liu, Y. Song, Q. F. Gu, D. L. Sun, L. F. Hu, *ACS Nano* **2018**, *12*, 2968.
[22] F. Song, X. L. Hu, *Nat. Commun.* **2014**, *5*, 4477.
[23] J. T. Zhang, Z. Li, Y. Chen, S. Y. Gao, X. W. Lou, *Angew. Chem., Int. Ed.* **2018**, *130*, 11110.
[24] J. M. Meng, Y. Song, Z. M. Qin, Z. H. Wang, X. J. Mu, J. Wang, X. X. Liu, *Adv. Funct. Mater.* **2022**, *32*, 2204026.
[25] R. Chen, S. F. Hung, D. J. Zhou, J. J. Gao, C. J. Yang, H. B. Tao, H. B. Yang, L. P. Zhang, L. L. Zhang, Q. H. Xiong, H. M. Chen, B. Liu, *Adv. Mater.* **2019**, *31*, 1903909.
[26] S. S. Bi, S. Wang, F. Yue, Z. W. Tie, Z. Q. Niu, *Nat. Commun.* **2021**, *12*, 6991.
[27] Z. Chang, H. J. Yang, Y. Qiao, X. Y. Zhu, P. Hu, H. S. Zhou, *Adv. Mater.* **2022**, *34*, 2201339.
[28] T. S. Mathis, N. Kurra, X. H. Wang, D. Pinto, P. Simon, Y. Gogotsi, *Adv. Energy Mater.* **2019**, *9*, 1902007.
[29] X. Y. Wu, Y. K. Xu, H. Jiang, Z. X. Wei, J. J. Hong, A. S. Hernandez, F. Du, X. L. Ji, *ACS Appl. Energy Mater.* **2018**, *1*, 3077.
[30] X. K. Zhang, M. T. Xia, T. T. Liu, N. Peng, H. X. Yu, R. T. Zheng, L. Y. Zhang, M. Shui, J. Shu, *Chem. Eng. J.* **2021**, *421*, 127767.
[31] Y. Ma, T. J. Sun, Q. S. Nian, S. B. Zheng, T. Ma, Q. R. Wang, H. H. Du, Z. L. Tao, *Nano Res.* **2022**, *15*, 2047.
[32] Y. D. Zhang, Y. F. An, B. Yin, J. M. Jiang, S. Y. Dong, H. Dou, X. G. Zhang, *J. Mater. Chem. A* **2019**, *7*, 11314.
[33] X. K. Zhang, M. T. Xia, H. X. Yu, J. W. Zhang, Z. W. Yang, L. Y. Zhang, J. Shu, *Nano-micro Lett.* **2021**, *13*, 139.
[34] Z. Z. Zhao, W. Zhang, M. Liu, D. Wang, X. Y. Wang, L. R. Zheng, X. Zou, Z. Z. Wang, D. B. Li, K. K. Huang, W. T. Zheng, *Energy Environ. Mater.* **2022**, https://doi.org/10.1002/eem2.12342.
[35] W. X. Hou, C. Yan, P. R. Shao, K. Dai, J. Yang, *Nanoscale* **2022**, *14*, 8501.
[36] J. H. Liu, W. H. Zhou, R. Z. Zhao, Z. D. Yang, W. Li, D. L. Chao, S. Z. Qiao, D. Y. Zhao, *J. Am. Chem. Soc.* **2021**, *143*, 15475.
[37] D. S. Charles, M. Feygenson, K. Page, J. Neuefeind, W. Q. Xu, X. W. Teng, *Nat. Commun.* **2017**, *8*, 15520.
[38] Y. X. Guo, W. Wang, H. P. Lei, M. Y. Wang, S. Q. Jiao, *Adv. Mater.* **2022**, *34*, 2110109.
[39] Q. G. Pan, Y. P. Zheng, Z. P. Tong, L. Shi, Y. B. Tang, *Angew. Chem., Int. Ed.* **2021**, *60*, 11835.
[40] D. L. Chao, W. H. Zhou, F. X. Xie, C. Ye, H. Li, M. Jaroniec, S. Z. Qiao, *Sci. Adv.* **2020**, *6*, 4098.
[41] C. Wang, Z. X. Pei, Q. Q. Meng, C. M. Zhang, X. Sui, Z. W. Yuan, S. J. Wang, Y. Chen, *Angew. Chem., Int. Ed.* **2021**, *60*, 990.
[42] X. S. Liu, W. H. Zuo, B. Z. Zheng, Y. X. Xiang, K. Zhou, Z. M. Xiao, P. Z. Shan, J. W. Shi, Q. Li, G. M. Zhong, R. Q. Fu, Y. Yang, *Angew. Chem., Int. Ed.* **2019**, *58*, 18086.
[43] R. Z. Ma, J. B. Liang, K. Takada, T. Sasaki, *J. Am. Chem. Soc.* **2011**, *133*, 613.
[44] I. Stoševski, A. Bonakdarpour, B. Z. Fang, P. Lo, D. P. Wilkinson, *Electrochim. Acta* **2021**, *390*, 138852.
[45] S. J. Pan, H. Li, D. Liu, R. Huang, X. L. Pan, D. Ren, J. Li, M. Shakouri, Q. X. Zhang, M. J. Wang, C. C. Wei, L. Q. Mai, B. Zhang, Y. Zhao, Z. B. Wang, M. Graetzel, X. D. Zhang, *Nat. Commun.* **2022**, *13*, 2294.
[46] E. S. Ilton, J. E. Post, P. J. Heaney, F. T. Ling, S. N. Kerisit, *Appl. Surf. Sci.* **2016**, *366*, 475.
[47] F. Y. Jing, Y. N. Liu, Y. R. Shang, C. D. Lv, L. L. Xu, J. Pei, J. Liu, G. Chen, C. S. Yan, *Energy Storage Mater.* **2022**, *49*, 164.
[48] S. P. Zankowski, L. V. Hoecke, F. Mattelaer, M. D. Raedt, O. Richard, C. Detavernier, P. M. Vereecken, *Chem. Mater.* **2019**, *31*, 4805.
[49] W. Guo, C. C. Dun, C. Yu, X. D. Song, F. P. Yang, W. Z. Kuang, Y. Y. Xie, S. F. Li, Z. Wang, J. H. Yu, G. S. Fu, J. H. Guo, M. A. Marcus, J. J. Urban, Q. Y. Zhang, J. S. Qiu, *Nat. Commun.* **2022**, *13*, 1409.
[50] S. L. Liu, M. H. Dong, Y. X. Wu, S. Luan, Y. Xin, J. Du, S. P. Li, H. Z. Liu, B. X. Han, *Nat. Commun.* **2022**, *13*, 2320.
[51] Q. S. Nian, J. Y. Wang, S. Liu, T. J. Sun, S. B. Zheng, Y. Zhang, Z. L. Tao, J. Chen, *Angew. Chem., Int. Ed.* **2019**, *58*, 16994.
[52] H. J. Lunk, H. Hartl, M. A. Hartl, M. J. G. Fait, I. G. Shenderovich, M. Feist, T. A. Frisk, L. L. Daemen, D. Mauder, R. Eckelt, A. A. Gurinov, *Inorg. Chem.* **2010**, *49*, 9400.
[53] M. T. Xia, X. K. Zhang, H. X. Yu, Z. W. Yang, S. Chen, L. Y. Zhang, M. Shui, Y. Xie, J. Shu, *Chem. Eng. J.* **2021**, *421*, 127759.
[54] L. Yan, Y. E. Qi, X. L. Dong, Y. G. Wang, Y. Y. Xia, *eScience* **2021**, *1*, 212.